Electron tunnelling in self-assembled monolayers

Wenyong Wang[1]**, Takhee Lee**[2] **and Mark A Reed**[3]

Departments of Electrical Engineering, Applied Physics, and Physics, Yale University,
PO Box 208284, New Haven, CT 06520, USA

E-mail: mark.reed@yale.edu

Abstract

A review on the mechanisms and characterization methods of electronic transport through self-assembled monolayers (SAMs) is presented. Using SAMs of alkanethiols in a nanometre scale device structure, tunnelling is unambiguously demonstrated as the main intrinsic conduction mechanism for defect-free large bandgap SAMs, exhibiting well-known temperature and length dependences. Inelastic electron tunnelling spectroscopy exhibits clear vibrational modes of the molecules in the device, presenting direct evidence of the presence of molecules in the device.

[1] Current address: Semiconductor Electronics Division, National Institute of Standards and Technology, Gaithersburg, MD 20899, USA.
[2] Current address: Department of Materials Science and Engineering, Gwangju Institute of Science and Technology, Gwangju, 500-712, Korea.
[3] Author to whom any correspondence should be addressed.

Contents

1. Introduction

The suggestion [1] and demonstration [2] of utilizing molecules as the active region of electronic devices has recently generated considerable interest in both basic transport physics and potential technological applications of 'molecular electronics' [3, 4]. However, some reports of molecular mechanisms in electronic devices [5, 6] have been shown to be premature and due to filamentary conduction [7], highlighting the fabrication sensitivity of molecular structures and the need to institute reliable controls and methods to validate true molecular transport [8]. A related problem is the characterization of molecules in the active device structure, including their configuration, bonding and indeed even their very presence. Here, we present results on well-understood molecular assemblies, which exhibit an understood classical transport behaviour, and which can be used as a control for eliminating (or understanding) fabrication variables. Utilizing tunnelling spectroscopic methods, we present the first unambiguous evidence of the presence of molecules in the junction, and further confirm the charge transport mechanism obtained by standard current–voltage characterizations.

A molecular system whose structure and configuration are sufficiently well-characterized such that it can serve as a standard is the extensively studied alkanethiol ($CH_3(CH_2)_{n-1}SH$) self-assembled monolayer (SAM) [9]. This system is useful as a control, since properly prepared SAMs form single van der Waals crystals [9, 10], and presents a simple classical metal–insulator–metal (M–I–M) tunnel junction when fabricated between metallic contacts due to the large HOMO–LUMO gap (HOMO: highest occupied molecular orbital, LUMO: lowest unoccupied molecular orbital) of approximately 8 eV [4] [11, 12].

Various surface analytical tools have been utilized to investigate the surface and bulk properties of the alkanethiol SAMs, such as x-ray photoelectron spectroscopy [13], Fourier transform infrared spectroscopy (FTIR) [14], Raman spectroscopy [15], scanning tunnelling microscopy (STM) [10], etc. For example, studies have shown that the bonding of the thiolate group to the gold surface is strong with a bonding energy of $\sim$1.7 eV [9]. STM topography examinations revealed that alkanethiols adopt the commensurate crystalline lattice characterized by a c(4 × 2) superlattice of a ($\sqrt{3} \times \sqrt{3}$)R30° [10, 16]. FTIR investigation showed that the orientation of the alkanethiol SAMs on Au(111) surfaces are tilted $\sim$30° from the surface normal [17].

Electronic transport through alkanethiol SAMs have also been characterized by STM [18, 19], conducting atomic force microscopy [20–23], mercury-drop junctions [24–27], cross-wire junctions [28], and electrochemical methods [29–31]. These investigations are exclusively at ambient temperature—clearly useful—but insufficient for an unambiguous claim that the transport mechanism is tunnelling (of course expected, assuming that the Fermi levels of the contacts lie within the large HOMO–LUMO gap). However, in the absence of temperature-dependent current–voltage ($I(V, T)$) characteristics, other conduction mechanisms (such as thermionic, hopping or filamentary conduction) cannot be excluded, which complicate the analysis, and thus such a claim is premature.

Utilizing a nanometre scale device structure that incorporates alkanethiol SAMs, we demonstrate devices that allow $I(V, T)$ and structure-dependent measurements [32, 33] with results that can be compared with accepted theoretical models of M–I–M tunnelling. The use of this fabrication approach is not special in any way (other than that we have so far found it to be successful)—indeed we stress that any successful device fabrication method should yield the results described below if one is characterizing the intrinsic molecular transport properties.

---

[4] Although the HOMO–LUMO gap of alkyl chain type molecules has been reported (see [12]), there is no experimental data on the HOMO–LUMO gap for Au/alkanethiol SAM/Au system. 8 eV is commonly used as HOMO–LUMO gap of alkanethiol.
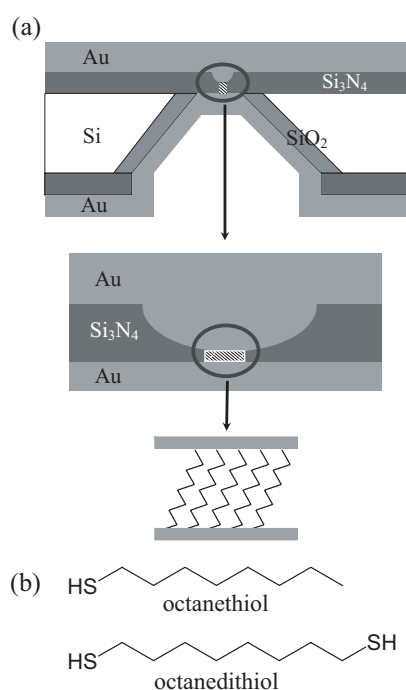
(a)

(b)

Figure 1. Schematics of a nanometre scale device used in this study (not drawn to scale in the relative thickness). (*a*) Top schematic is the cross section of a silicon wafer with a nanometre scale pore etched through a suspended silicon nitride membrane. Middle and bottom schematics show a Au/SAM/Au junction formed in the pore area. (*b*) The structures of octanethiol and octanedithiol are shown as examples.

The electronic transport is further investigated with the technique of inelastic electron tunnelling spectroscopy (IETS) [33]. IETS was developed in the 1960s as a powerful spectroscopic tool to study the vibrational spectrum of organic molecules confined inside metal–oxide–metal junctions [34–38]. In this study, IETS is utilized for the purpose of molecule identification, chemical bonding and conduction mechanism investigations of the 'control' SAMs. The exclusive presence of well-known vibrational modes of the alkanes used are direct evidence of the molecules in the device structure, something that has to date only been inferred (with good reason, but nonetheless not unambiguously). The vibrational modes, exclusively identified as alkanes (as well as contact modes) are difficult to interpret in any other way other than as components in the active region of the device. The inelastic tunnelling spectra also demonstrate that electronic tunnelling occurs through the molecules, confirming the conduction mechanism obtained by $I(V, T)$ characterizations. The specific spectral lines also yield intrinsic linewidths that may give insight into molecular conformation, and may prove to be a powerful tool in future molecular device characterization.

2. Experiment

Electronic transport measurements on alkanethiol SAMs were performed using a device structure similar to that reported previously [32, 33, 39–41]. In this device, as illustrated in figure 1(*a*) (not drawn to scale in the relative thickness), a number of molecules (approximately several thousands) are sandwiched between two metallic contacts. This technique provides a
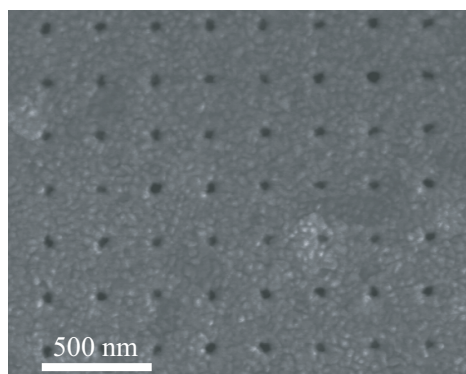
Figure 2. A SEM image of a representative array of pores used to calibrate device size. The scale bar is 500 nm.

stable device structure and makes cryogenic measurements possible. The device fabrication starts with a high resistivity silicon wafer with low stress Si_3N_4 film deposited on both sides by low pressure chemical vapour deposition (LPCVD). By standard photolithography processing, a suspended Si_3N_4 membrane (size of $40\,\mu m \times 40\,\mu m$ and thickness of ~ 70 nm) is fabricated on the top of the wafer. Subsequent e-beam lithography and reactive ion etching creates a single pore with a diameter of tens of nanometres through the membrane. As the next step, 150 nm gold is thermally evaporated onto the top of the wafer to fill the pore and form one of the metallic contacts.

The device is then transferred into a molecular solution to deposit the SAM layer. For our experiments, $a \sim 5$ mM alkanethiol solution is prepared by adding $\sim 10\,\mu L$ alkanethiols into 10 mL ethanol[5]. The deposition is done in solution for 24 h inside a nitrogen filled glove box with an oxygen level of less than 100 ppm. Three alkanemonothiol molecules of different molecular lengths—octanethiol ($CH_3(CH_2)_7SH$; denoted as C8, for the number of alkyl units), dodecanethiol ($CH_3(CH_2)_{11}SH$, denoted as C12), and hexadecanethiol ($CH_3(CH_2)_{15}SH$, denoted as C16)—and one alkanedithiol molecule—octanedithiol ($HS(CH_2)_8SH$, denoted as C8-dithiol)—were used to form the active molecular components[4]. As representative examples, the chemical structures of octanethiol and octanedithiol are shown in figure 1(*b*).

In order to statistically determine the pore size, test patterns (arrays of pores) were created under similar fabrication conditions. Figure 2 shows a scanning electron microscope (SEM) image of such test pattern arrays. This indirect measurement of device size is done since SEM examination of the actual device can cause hydrocarbon contamination of the device and subsequent contamination of the monolayer. From regression analysis of 298 pores, the device sizes of the C8, C12, C16, and C8-dithiol samples are determined as 50 ± 8 nm, 45 ± 2 nm, 45 ± 2 nm, and 51 ± 5 nm in diameters, respectively. A more ideal (less parasitic) C8 sample supercedes that of previous reports [32], and derived parameters from the two data sets agree to within a standard error. We will use these device areas as the effective contact areas. Although one could postulate that the actual area of metal that contacts the molecules may be different, there is little reason to propose it would be different as a function of length over the range of alkanethiols used, and at most would be a constant systematic error.

The sample is then transferred in ambient conditions to an evaporator that has a cooling stage to deposit the opposing Au contact. During the thermal evaporation (under a pressure of $\sim 10^{-8}$ Torr), liquid nitrogen is kept flowing through the cooling stage in order to avoid

---

[5] Ethanol and alkane molecules were purchased from Sigma-Aldrich.

Table 1. Possible conduction mechanisms; adapted from [44].

Conduction mechanism	Characteristic behaviour	Temperature dependence	Voltage dependence
Direct tunnelling[a]	$J \sim V \exp\left(-\dfrac{2d}{\hbar}\sqrt{2m\Phi}\right)$	None	$J \sim V$
Fowler–Nordheim tunnelling	$J \sim V^2 \exp\left(-\dfrac{4d\sqrt{2m}\,\Phi^{3/2}}{3q\hbar V}\right)$	None	$\ln\left(\dfrac{J}{V^2}\right) \sim \dfrac{1}{V}$
Thermionic emission	$J \sim T^2 \exp\left(-\dfrac{\Phi - q\sqrt{qV/4\pi\varepsilon d}}{k_B T}\right)$	$\ln\left(\dfrac{J}{T^2}\right) \sim \dfrac{1}{T}$	$\ln(J) \sim V^{1/2}$
Hopping conduction	$J \sim V \exp\left(-\dfrac{\Phi}{k_B T}\right)$	$\ln\left(\dfrac{J}{V}\right) \sim \dfrac{1}{T}$	$J \sim V$

[a] This characteristic of direct tunnelling is valid for the low bias regime (see equation (3a)).

thermal damage to the molecular layer [32, 42]. This technique reduces the kinetic energy of evaporated Au atoms at the surface of the monolayer, thus preventing Au atoms from punching through the monolayer. For the same reason, the evaporation rate is kept very low. For the first 10 nm of gold evaporated, the rate is less than 0.1 Å s^{-1}. Then, the rate is increased slowly to 0.5 Å s^{-1} for the rest of the evaporation and a total of 200 nm of gold is deposited to form the contact.

The device is subsequently packaged and loaded into a low temperature cryostat. The sample temperature is varied from 300 to 4.2 K by flowing cryogen vapour onto the sample (and thermometer) using a closed loop temperature controller. Two-terminal dc $I(V)$ measurements are performed using a semiconductor parameter analyser. Inelastic electron tunnelling spectra are obtained via a standard lock-in second harmonic measurement technique [34, 35]. A synthesized function generator is used to provide both the modulation and the lock-in reference signal. The second harmonic signal (proportional to $d^2 I/dV^2$) is directly measured using a lock-in amplifier, which is checked to be consistent with a numerical derivative of the first harmonic signal (proportional to dI/dV). Various modulation amplitudes and frequencies are utilized to obtain the spectra. The ac modulation is added to a dc bias using operational amplifier-based custom circuitry [43].

3. Theoretical basis

3.1. Possible conduction mechanisms

In table 1, possible conduction mechanisms are listed with their characteristic current, temperature and voltage-dependences [44]. (We do not discuss filamentary tunnelling mechanisms, which are easier to categorize [45].) Based on whether thermal activation is involved, the conduction mechanisms fall into two distinct categories: (i) thermionic or hopping conduction which has temperature-dependent $I(V)$ behaviour and (ii) direct tunnelling or Fowler–Nordheim tunnelling, which does not have temperature-dependent $I(V)$ behaviour. For example, thermionic and hopping conductions have been observed for 4-thioacetylbiphenyl SAMs [39] and 1,4-phenelyene diisocyanide SAMs [40]. On the other hand, the conduction mechanism is expected to be tunnelling when the Fermi levels of contacts lie within the large HOMO–LUMO gap for short length molecules, as for the case of alkanethiol molecular system [11, 12]. Previous work on Langmuir–Blodgett alkane monolayers [46] exhibited a significant impurity-dominated transport component, complicating the analysis. $I(V)$ measurements on self-assembled alkanethiol monolayers have also been reported [18–28, 47]; however, all of

these measurements were performed at fixed temperature (300 K), which is insufficient to prove tunnelling as the dominant mechanism.

3.2. Tunnelling models

To describe the transport through a molecular system having HOMO and LUMO energy levels, one of the models that can be applied is the Franz two-band model [48–51]. This model provides a non-parabolic energy-momentum $E(k)$ dispersion relationship by considering the contributions of both the HOMO and LUMO energy levels [48]:

$$k^2 = \frac{2m^*}{\hbar^2} E \left(1 + \frac{E}{E_{\mathrm{g}}} \right), \tag{1}$$

where k is the imaginary part of the wave vector of electrons, m^* the electron effective mass, $h \ (=2\pi\hbar)$ the Planck's constant, E the electron energy and E_{g} is the HOMO–LUMO energy gap. From this non-parabolic $E(k)$ relationship, the effective mass of the electron tunnelling through the SAM can be deduced if we know the barrier height of the metal–SAM–metal junction.

When the Fermi level of the metal is aligned close enough to one energy level (either HOMO or LUMO), the effect of the other distant energy level on the tunnelling transport is negligible, and the widely used Simmons model [52] is an excellent approximation [53]. The Simmons model expresses the tunnelling current density through a barrier in the tunnelling regime of $V < \Phi_{\mathrm{B}}/e$ as [24, 52]

$$J = \frac{e}{4\pi^2 \hbar \, d^2} \left\{ \left(\Phi_{\mathrm{B}} - \frac{eV}{2} \right) \exp \left[-\frac{2(2m)^{1/2}}{\hbar} \alpha \left(\Phi_{\mathrm{B}} - \frac{eV}{2} \right)^{1/2} d \right] \right.$$
$$\left. - \left(\Phi_{\mathrm{B}} + \frac{eV}{2} \right) \exp \left[-\frac{2(2m)^{1/2}}{\hbar} \alpha \left(\Phi_{\mathrm{B}} + \frac{eV}{2} \right)^{1/2} d \right] \right\}, \tag{2}$$

where m is the electron mass, d the barrier width, Φ_{B} the barrier height and V is the applied bias. For molecular systems, the Simmons model has been modified with a parameter α [24, 32]. α is a unitless adjustable parameter that is introduced to provide either a way of applying the tunnelling model of a rectangular barrier to tunnelling through a nonrectangular barrier [24], or an adjustment to account for the effective mass (m^*) of the tunnelling electrons through a rectangular barrier [24, 32, 51, 54], or both. $\alpha = 1$ corresponds to the case for a rectangular barrier and bare electron mass. By fitting individual $I(V)$ data using equation (2), Φ_{B} and α values can be obtained.

Equation (2) can be approximated in two limits: low bias and high bias as compared with the barrier height Φ_{B}. For the low bias range, equation (2) can be approximated as [52]

$$J \approx \left(\frac{(2m\Phi_{\mathrm{B}})^{1/2} e^2 \alpha}{h^2 d} \right) V \exp \left[-\frac{2(2m)^{1/2}}{\hbar} \alpha (\Phi_{\mathrm{B}})^{1/2} d \right]. \tag{3a}$$

To determine the high bias limit, we compare the relative magnitudes of the first and second exponential terms in equation (2). At high bias, the first term is dominant and thus the current density can be approximated as

$$J \approx \left(\frac{e}{4\pi^2 \hbar d^2} \right) \left(\Phi_{\mathrm{B}} - \frac{eV}{2} \right) \exp \left[-\frac{2(2m)^{1/2}}{\hbar} \alpha \left(\Phi_{\mathrm{B}} - \frac{eV}{2} \right)^{1/2} d \right]. \tag{3b}$$

The tunnelling currents in both bias regimes are exponentially dependent on the barrier width d. In the low bias regime the tunnelling current density is $J \propto (1/d) \exp(-\beta_0 d)$, where
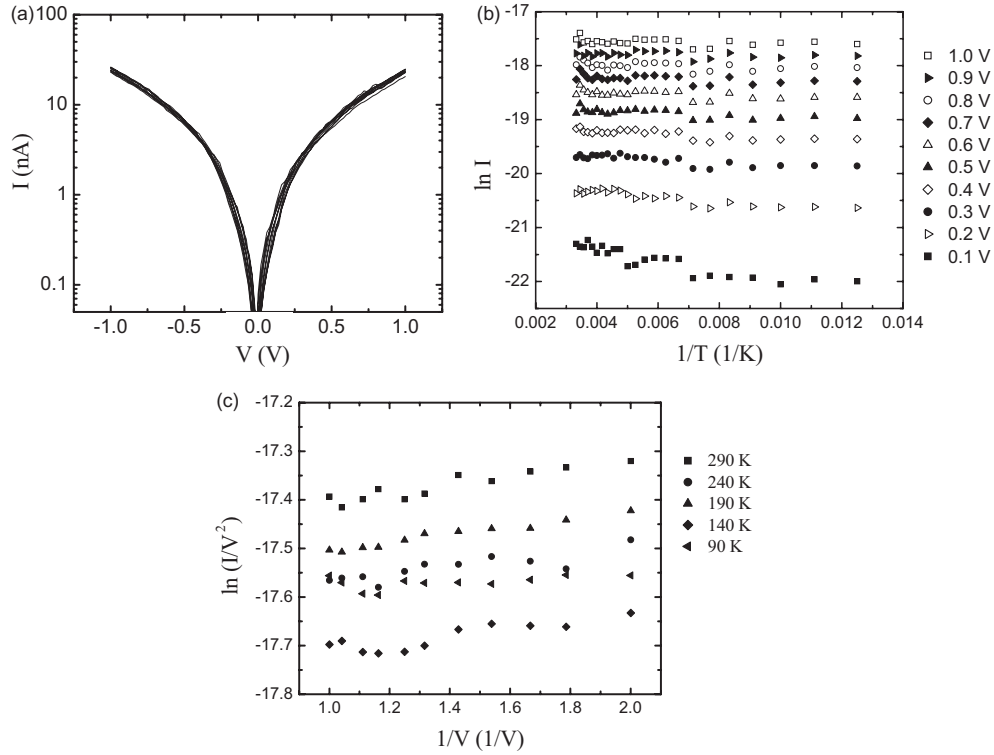
Figure 3. (*a*) Temperature-dependent $I(V)$ characteristics of dodecanethiol (C12). $I(V)$ data at temperatures from 300 to 80 K with 20 K steps are plotted on a log scale. (*b*) Arrhenius plot generated from the $I(V)$ data in (*a*), at voltages from 0.1 to 1.0 V with 0.1 V steps. (*c*) Plot of $\ln(I/V^2)$ versus $1/V$ at selected temperatures.

β_0 is the bias-independent decay coefficient:

$$\beta_0 = \frac{2(2m)^{1/2}}{\hbar}\alpha(\Phi_B)^{1/2}, \tag{4a}$$

while in the high bias regime, $J \propto (1/d^2)\exp(-\beta_V d)$, where β_V is the bias-dependent decay coefficient:

$$\beta_V = \frac{2(2m)^{1/2}}{\hbar}\alpha\left(\Phi_B - \frac{eV}{2}\right)^{1/2} = \beta_0\left(1 - \frac{eV}{2\Phi_B}\right)^{1/2}. \tag{4b}$$

At high bias, β_V decreases as the bias increases, which results from the barrier lowering effect due to the applied bias.

4. Results

4.1. Tunnelling current–voltage characteristics

4.1.1. Temperature-variable current–voltage (I(V, T)) measurement. In order to determine the conduction mechanism of self-assembled alkanethiol molecular systems, $I(V)$ measurements in a sufficiently wide temperature range (300–80 K) and resolution (10 K) were performed. Figure 3(*a*) shows a representative $I(V, T)$ characteristic of dodecanethiol (C12)

measured with the device structure as shown in figure 1(*a*). Positive bias corresponds to electrons injected from the physisorbed Au contact (bottom contact in figure 1(*a*)) into the molecules. By using the contact area of 45 ± 2 nm in diameter determined from SEM study, a current density of 1500 ± 200 A cm^{-2} at 1.0 V is determined. No significant temperature dependence of the characteristics (from $V = 0$ to 1.0 V) is observed over the range from 300 to 80 K. An Arrhenius plot ($\ln(I)$ versus $1/T$) of this is shown in figure 3(*b*), exhibiting little temperature dependence in the slopes of $\ln(I)$ versus $1/T$ at different bias, thus indicating the absence of thermal activation. Therefore, we conclude that the conduction mechanism through alkanethiol is tunnelling contingent on demonstrating a correct molecular length dependence. The tunnelling through alkanethiol SAMs has been assumed as 'through-bond' tunnelling, i.e. along the tilted molecular chains between the metal contacts [21, 22, 31, 55]. Based on the applied bias as compared with the barrier height (Φ_B), the tunnelling through a SAM layer can be categorized into either direct ($V < \Phi_B/e$) or Fowler–Nordheim ($V > \Phi_B/e$) tunnelling. These two tunnelling mechanisms can be distinguished due to their distinct voltage dependences (see table 1). Analysis of $\ln(I/V^2)$ versus $1/V$ (in figure 3(*c*)) shows no significant voltage dependence, indicating no obvious Fowler–Nordheim transport behaviour in this bias range (0–1.0 V) and thus determining that the barrier height is larger than the applied bias, i.e. $\Phi_B > 1.0$ eV. This study is restricted to applied biases $\leqslant 1.0$ V and the transition from direct to Fowler–Nordheim tunnelling requires higher bias.

The importance of variable temperature measurements to validate tunnelling is demonstrated in figure 4. Here, the $I(V)$ of an octanethiol (C8) device is shown (figure 4(*a*)), whose $I(V)$ shape looks very similar to figure 3 (i.e. direct tunnelling), and indeed can be fit to a Simmons model. However, further $I(V, T)$ measurements display an obvious temperature dependence (figure 4(*b*)), which can be fit well to a hopping conduction model (table 1) with a well-defined activation energy of 190 meV (figure 4(*c*)). This and other similar impurity-mediated transport phenomena (such as Coulomb blockade) are observed in a subset of devices, and are indicative of the unintentional incorporation of a trap or defect level in those devices. This study instead focuses on devices that do not show any defect-mediated transport and probes the intrinsic behaviour of the molecular layer.

Having established tunnelling as the conduction mechanism in a device, we will now obtain the barrier height by comparing experimental $I(V)$ data with theoretical calculations from tunnelling models.

4.1.2. Tunnelling characteristics through alkanethiols. From the modified Simmons model (equation (2)) by adjusting two parameters Φ_B and α, a nonlinear least squares fitting can be performed to fit the measured C12 $I(V)$ data (calculation assuming $\alpha = 1$ has been previously shown not to fit $I(V)$ data well for some alkanethiol measurements at fixed temperature (300 K)) [24]. By using a device that is 45 nm in diameter, the best fitting parameters (minimizing χ^2) for the room temperature C12 $I(V)$ data were found to be $\Phi_B = 1.42 \pm 0.04$ eV and $\alpha = 0.65 \pm 0.01$, where the error ranges of Φ_B and α are dominated by potential device size fluctuations of 2 nm. Likewise, data sets were obtained and fittings were done for octanethiol (C8) and hexadecanethiol (C16), which yielded values {$\Phi_B = 1.83 \pm 0.10$ eV and $\alpha = 0.61 \pm 0.01$} and {$\Phi_B = 1.40 \pm 0.03$ eV and $\alpha = 0.68 \pm 0.01$}, respectively.

Using $\Phi_B = 1.42$ eV and $\alpha = 0.65$, a calculated $I(V)$ for C12 is plotted as a solid curve on a linear scale (figure 5(*a*)) and on a semi-log scale (figure 5(*b*)). A calculated $I(V)$ for $\alpha = 1$ and $\Phi_B = 0.65$ eV (which gives the best fit at low bias range) is shown as the dashed curve in the same figure, illustrating that with $\alpha = 1$ only limited regions of the $I(V)$ can be fit (specifically here, for $V < 0.3$ V). For the case of a rectangular barrier, the α parameter fit presented above corresponds to an effective mass m^* $(=\alpha^2 m)$ of 0.42 m.
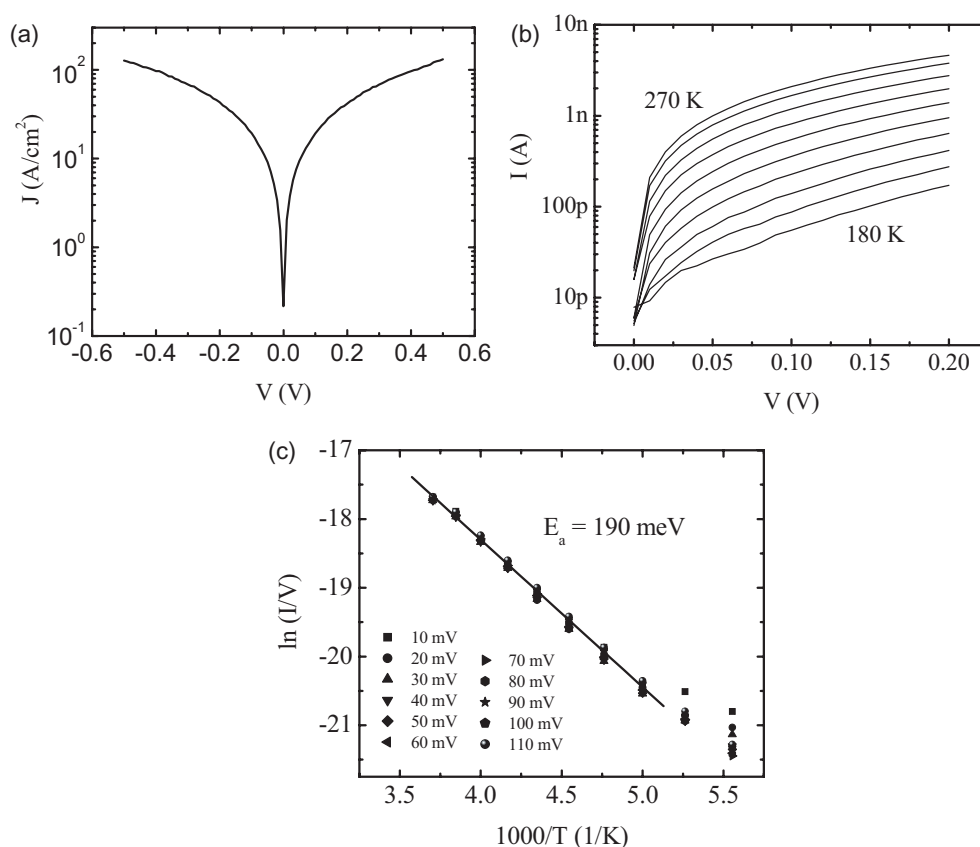
Figure 4. (*a*) $I(V)$ characteristics of an octanethiol (C8) device at 270 K. (*b*) Temperature dependence of the device from 270 to 180 K (in 10 K increments). (*c*) Plot of $\ln(I/V)$ versus $1/T$ at various voltages. The activated behaviour is bias voltage independent, thus the behaviour is hopping (in this device) due to incorporation of a defect of energy 190 meV. This class of devices is not suitable for investigation of the intrinsic transport mechanism in the SAM as it is dominated by a defect.

In order to investigate the dependence of the Simmons model fitting on Φ_B and α, a fitting minimization analysis was undertaken on the individual Φ_B and α values, as well as their product form of $\alpha\Phi_B^{1/2}$ in equation (4*a*). $\Delta(\Phi_B, \alpha) = (\Sigma|I_{\exp,V} - I_{\text{cal},V}|^2)^{1/2}$ was calculated and plotted, where $I_{\exp,V}$ are the experimental current–voltage values and $I_{\text{cal},V}$ is calculated using equation (2); 7500 different $\{\Phi_B, \alpha\}$ pairs were used in the fittings, with Φ_B ranging from 1.0 to 2.5 eV (0.01 eV increment) and α from 0.5 to 1.0 (0.01 increment). Figure 6(*a*) is a representative contour plot of $\Delta(\Phi_B, \alpha)$ versus Φ_B and α values generated for the C12 $I(V)$ data where darker regions correspond to smaller $\Delta(\Phi_B, \alpha)$ and various shades represent half order of magnitude $\Delta(\Phi_B, \alpha)$ steps. The darker regions represent better fits of equation (2) to the measured $I(V)$ data. In the inset in figure 6(*a*) one can see there is a range of possible Φ_B and α values yielding minimum fitting parameters. Although the tunnelling parameters determined from the previous Simmons tunnelling fitting $\{\Phi_B = 1.42\,\text{eV}$ and $\alpha = 0.65\}$ lie within this minimum region in this figure, there is a distribution of other possible values.

A plot of $\Delta(\Phi_B, \alpha)$ versus $\alpha\Phi_B^{1/2}$ for the same device reveals a more pronounced dependence, and is shown in figure 6(*b*). This plot indicates that the fitting to the Simmons
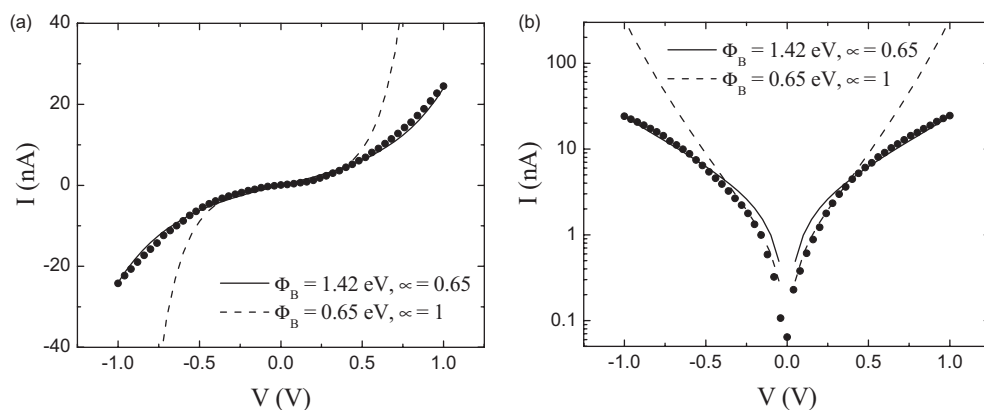
Figure 5. Measured C12 $I(V)$ data ($\bullet$) are compared with calculation (——) using the optimum fitting parameters of $\Phi_B = 1.42\,\text{eV}$ and $\alpha = 0.65$. The calculated $I(V)$ from a simple rectangular model ($\alpha = 1$) with $\Phi_B = 0.65\,\text{eV}$ is also shown as the dashed curve. Current is plotted (a) on a linear scale and (b) on a log scale.
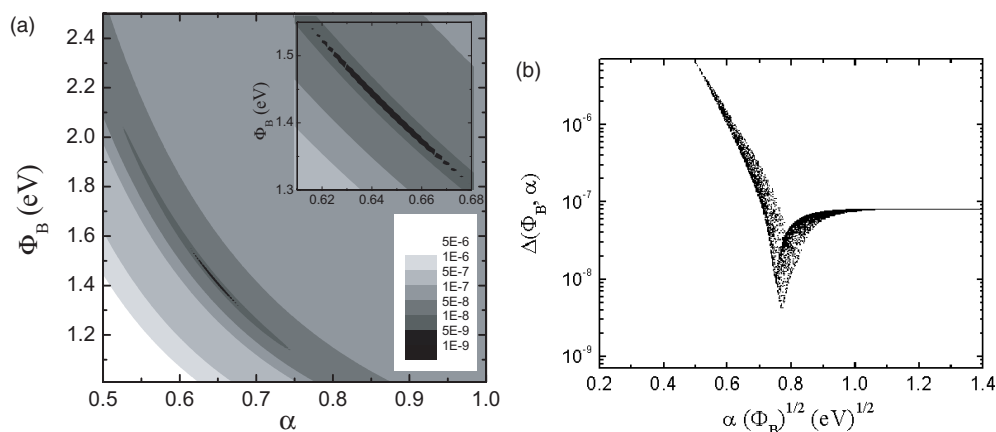

Figure 6. (a) Contour plot of $\Delta(\Phi_B, \alpha)$ values for a C12 nanopore device as a function of Φ_B and α, where the darker region corresponds to a better fitting. Inset shows detailed minimization fitting regions. (b) A plot of $\Delta(\Phi_B, \alpha)$ as a function of $\alpha\Phi_B^{1/2}$.

model sharply depends on the product $\alpha\Phi_B^{1/2}$. For this plot, the $\Delta(\Phi_B, \alpha)$ is minimized at $\alpha\Phi_B^{1/2}$ of $0.77\,(eV)^{1/2}$ corresponding to a β_0 value of $0.79\,\text{Å}^{-1}$ from equation (4a). The C8 and C16 devices showed similar results, indicating that the Simmons tunnelling model has a strong $\alpha\Phi_B^{1/2}$ dependence. For the C8 device, although Φ_B obtained from the fitting is a little larger, combined α and Φ_B gives a similar β_0 value within the error range as the C12 and C16 devices (table 2).

4.1.3. Length-dependent tunnelling through alkanethiols. Three alkanethiols of different molecular length, C8, C12 and C16, were investigated to study length-dependent tunnelling behaviour. Figure 7 is a semi-log plot of tunnelling current densities multiplied by molecular length (Jd at low bias and Jd^2 at high bias) as a function of the molecular length for these alkanethiols. The molecular lengths used in this plot are 13.3 Å, 18.2 Å and 23.2 Å for C8,

Table 2. Summary of alkanethiol tunnelling parameters in this study.

Molecules	J at 1 V (A cm^{-2})	Φ_B (eV)	α	m^a (m)	β_0 (Å^{-1})^a
C8	$31\,000 \pm 10\,000$	1.83 ± 0.10	0.61 ± 0.01	0.37	0.85 ± 0.04
C12	$1\,500 \pm 200$	1.42 ± 0.04	0.65 ± 0.01	0.42	0.79 ± 0.02
C16	23 ± 2	1.40 ± 0.03	0.68 ± 0.01	0.46	0.82 ± 0.02
C8-dithiol	$93\,000 \pm 18\,000$	1.20 ± 0.03	0.59 ± 0.01	0.35	0.66 ± 0.02

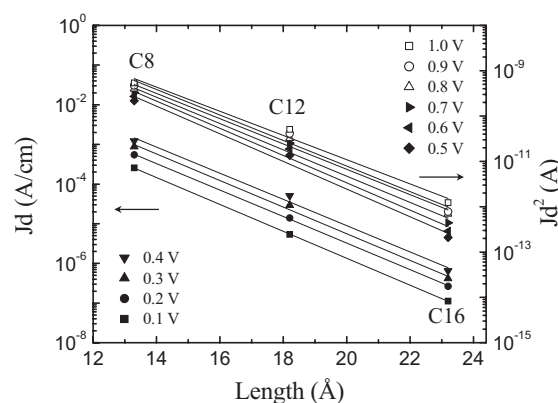^{a} β_0 values were calculated using equation (4a).

Figure 7. Log plot of tunnelling current densities multiplied by molecular length d at low bias and by d^2 at high bias (symbols) versus molecular lengths. The lines through the data points are linear fittings.

C12 and C16, respectively. Each molecular length was determined by adding an Au-thiol bonding length to the length of molecule [21]. Note that these lengths assume through-bond tunnelling [21, 22, 31, 55]. The high and low bias regimes are defined somewhat arbitrarily by comparing the relative magnitudes of the first and second exponential terms in equation (2). Using $\Phi_B = 1.42$ eV and $\alpha = 0.65$ obtained from nonlinear least squares fitting of the C12 $I(V)$ data, the second term becomes less than $\sim$10% of the first term at $\sim$0.5 V, which is chosen as the boundary of low and high bias ranges.

As seen in figure 7, the tunnelling current shows an exponential dependence on molecular length, which is consistent with the Simmons tunnelling model (equation (3)). The β values can be determined from the slope at each bias and are plotted in figure 8. The error bar of an individual β value in this plot was obtained by considering both the device size uncertainties and the linear fitting errors.

The β values determined are almost independent of bias in the low bias range ($V \lesssim 0.5$ V), and an average β of 0.77 ± 0.06 Å^{-1} in this region (from 0 to 0.5 V) can be calculated from figure 8. Table 3 is a summary of previously reported alkanethiol transport parameters obtained by different techniques. The current densities (J) listed in table 3 are for C12 monothiol or dithiol devices at 1 V, which are extrapolated from published results of other length alkane molecules. The large variation of J in these reports can be attributed to the uncertainties in device contact geometry and junction area, as well as complicating inelastic or defect contributions. The β value (0.77 ± 0.06 Å$^{-1} \approx 0.96 \pm 0.08$ per methylene) for alkanethiols reported here is comparable to previously reported values, as summarized in table 3. This β value agrees with the value of 0.79 Å^{-1} (β_0) calculated via equation (4a) from fitting an
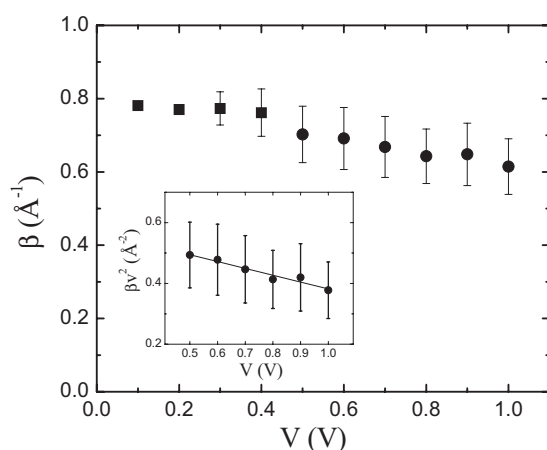
Figure 8. Plot of β versus bias in the low bias range ($\blacksquare$) and high bias ranges ($\bullet$). The inset shows a plot of β_V^2 versus bias with a linear fitting.

Table 3. Summary of alkanethiol tunnelling characteristic parameters.

Junction	β (Å^{-1})	J (A cm^{-2}) at 1 V	Φ_B (eV)	Technique	Ref.
(Bilayer) monothiol	0.87 ± 0.1	25–200[a]	2.1[e]	Hg-junction	[24]
(Bilayer) monothiol	0.71 ± 0.08	0.7–3.5[a]		Hg-junction	[26]
Monothiol	0.79 ± 0.01	1500 ± 200[b]	1.4[e]	Solid M–I–M	[32]
Monothiol	1.2			STM	[18]
Dithiol	0.8 ± 0.08	$(3.7–5) \times 10^{5}$[c]	5 ± 2[f]	STM	[19]
Monothiol	0.73–0.95	1100–1900[d]	2.2[e]	CAFM	[20]
Monothiol	0.64–0.8	10–50[d]	2.3[e]	CAFM	[22]
Dithiol	0.46 ± 0.02	$(3–6) \times 10^{5}$[c]	1.3–1.5[e]	CAFM	[23]
Monothiol	1.37 ± 0.03		1.8[f]	Tuning fork AFM	[47]
Monothiol	0.97 ± 0.04			Electrochemical	[29]
Monothiol	0.85			Electrochemical	[30]
Monothiol	0.91 ± 0.08			Electrochemical	[31]
Monothiol	0.76	2×10^{4} (at 0.1 V)[c]	1.3–3.4[g]	Theory	[56]
Monothiol	0.76			Theory	[57]
Monothiol	0.79			Theory	[54]

Note.
Some decay coefficients β were converted into the unit of Å^{-1} from the unit of per methylene.
The junction areas were estimated by optical microscope[a], SEM[b], assuming single molecule[c] and Hertzian contact theory[d].
Current densities (J) for C12 monothiol or dithiol at 1 V are extrapolated from published results for other length molecules by using conductance $\propto \exp(-\beta d)$ relationship.
Barrier height Φ_B values were obtained from Simmons equation[e], bias-dependence of β[f] and a theoretical calculation[g].

individual $I(V)$ characteristic of the C12 device. The calculated β_0 of C8 and C16 devices also have similar values, as summarized in table 2.

According to equation (4b), β_V^2 depends on the bias V linearly in the high bias range. The inset in figure 8 is a plot of β_V^2 versus V in this range (0.5–1.0 V) along with linear fitting of the data. From this fitting, $\Phi_B = 1.35 \pm 0.20$ eV and $\alpha = 0.66 \pm 0.04$ were obtained from the intercept and the slope, respectively, consistent with the values $\{\Phi_B = 1.42$ eV and $\alpha = 0.65\}$ obtained from the nonlinear least squares fitting in the previous section.
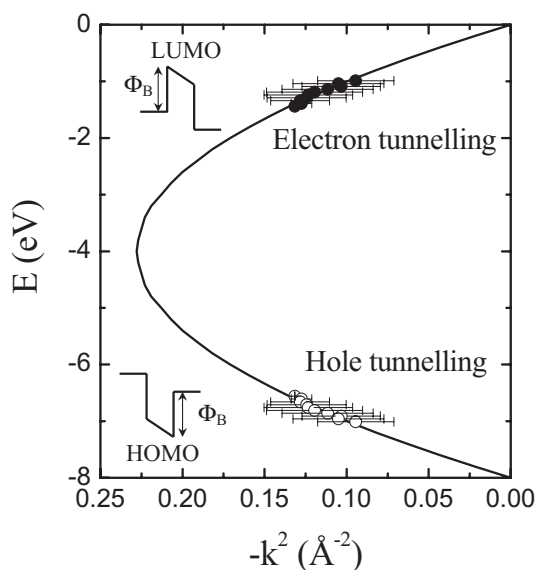
Figure 9. $E(k)$ relationship ($\bullet$, $\circ$) generated from the length-dependent measurement data for alkanethiols. Solid and open symbols correspond to electron and hole tunnelling, respectively. The insets show the corresponding energy band diagrams. The solid curve is the Franz two-band expression for $m^* = 0.43$ m.

β values for alkanethiols obtained by various experimental techniques have previously been reported and are summarized in table 3 [18–32, 47]. In order to compare with these reported β values, we also performed length-dependent analysis on our experimental data according to the generally used equation [19–27, 32]:

$$G = G_0 \exp(-\beta d). \tag{5}$$

This gives a β value from 0.84 to 0.73 Å^{-1} in the bias range from 0.1 to 1.0 V, which is comparable to results reported previously. For example, Holmlin *et al* [24] reported a β value of 0.87 Å^{-1} by mercury drop experiments, and Wold *et al* [20] have reported β of 0.94 Å^{-1} and Cui *et al* [22] reported β of 0.64 Å^{-1} for various alkanethiols by using a conducting atomic force microscope technique. These reported β were treated as bias-independent quantities, contrary to the results reported here and that observed in a slightly different alkane system (ligand-encapsulated nanoparticle/alkane-dithiol molecules) [23]. We also caution against the use of parameters that have not been checked with a temperature-dependent analysis, since small non-tunnelling components can dramatically affect the derived values of β.

4.1.4. Franz model. We have analysed our experimental data using a Franz two-band model [48–51]. Since there are no reliable experimental data on the Fermi level alignment in these metal–SAM–metal systems, Φ_B and m^* are treated as adjustable parameters. We performed a least squares fit on our data with the Franz non-parabolic $E(k)$ relationship (equation (1)) using an alkanethiol HOMO–LUMO gap of 8 eV[3] [12]. Figure 9 shows the resultant $E(k)$ relationship and the corresponding energy band diagrams. The zero of energy in this plot was chosen as the LUMO energy. The best fitting parameters obtained by minimizing χ^2 were $\Phi_B = 1.49 \pm 0.51$ eV and $m^* = 0.43 \pm 0.15$ m, where the error

ranges of Φ_B and m^* are dominated by the error fluctuations of β [$k^2 = -(\beta/2)^2$]. Both electron tunnelling near the LUMO and hole tunnelling near the HOMO can be described by these parameters. $\Phi_B = 1.49$ eV indicates that the Fermi level is aligned close to one energy level in either case; therefore, the Simmons model is a valid approximation. The Φ_B and m^* values obtained here are in reasonable agreement with the previous results obtained from the Simmons model.

4.2. Inelastic tunnelling

4.2.1. Inelastic electron tunnelling spectroscopy.

Electronic transport through alkanethiol SAMs is further investigated with the technique of IETS [33], such as that given in the works of 1966 by Jaklevic and Lambe [34], who studied the conductance of tunnel junctions with encased organic molecules. Since then it has become a powerful spectroscopic tool for chemical identification, chemical bonding investigation, and surface chemistry and physics studies [37]. In an inelastic tunnelling process the electron loses energy to a localized vibrational mode with a frequency ν when the applied bias satisfies the condition $eV = h\nu$. As a result, an additional tunnelling channel is opened for the electron, resulting in an increase in the total current at the applied bias corresponding to the vibrational mode energy [36]. Typically, only a small fraction of tunnelling electrons are involved in the inelastic tunnelling process (determined by the electron—vibronic mode coupling coefficient), resulting in a small conductance change, which is usually measured in the second harmonics of a phase-sensitive detector that yields the characteristic frequencies of the corresponding vibrational modes as well as other information [35–37].

$I(V, T)$ measurements and additional IETS studies have been performed on an octanedithiol (C8-dithiol) SAM using the aforementioned device structure shown in figure 1(a) [33]. Figure 10(a) is the $I(V, T)$ data for this device obtained from 300 to 4.2 K. An Arrhenius plot shown in figure 10(b) exhibits little temperature dependence, verifying that tunnelling is the main transport mechanism for C8-dithiol SAM. This result is in good agreement with the tunnelling transport characteristics observed previously. Figure 10(c) shows the room temperature $I(V)$ measurement result. Using a junction area of 51 ± 5 nm in diameter (obtained from statistical studies of the nanopore size with SEM), a current density of $(9.3 \pm 1.8) \times 10^4$ A cm^{-2} at 1.0 V is calculated. As a comparison, the current density of $(3.1 \pm 1.0) \times 10^4$ A cm^{-2} at 1.0 V was observed for C8 monothiol SAM. Using the modified Simmons model (equation (2)), the transport parameters of $\Phi_B = 1.20 \pm 0.03$ eV and $\alpha = 0.59 \pm 0.01$ ($m^* = 0.34$ m) were obtained for this C8-dithiol SAM.

Figure 11 shows the IETS spectrum of the same C8-dithiol SAM device obtained at $T = 4.2$ K. An ac modulation of 8.7 mV (rms value) at a frequency of 503 Hz was applied to the sample to acquire the second harmonic signals. The spectra are stable and repeatable upon successive bias sweeps. The spectrum at 4.2 K is characterized by three pronounced peaks in the 0–200 mV region at 33, 133 and 158 mV. From comparison with previously reported infrared (IR), Raman, and high resolution electron energy loss (HREEL) spectra of SAM covered gold surfaces (table 4), these three peaks are assigned to the ν(Au–S), ν(C–C) and γ_w(CH$_2$) modes of a surface bound alkanethiolate[6] [58–60]. The absence of a strong ν(S–H) signal at $\sim$329 mV suggests that most of the thiol groups have reacted with the gold bottom and top contacts. Peaks are also reproducibly observed at 80, 107 and 186 mV. They correspond to ν(C–S), δ_r(CH$_2$) and δ_s(CH$_2$) modes. The stretching mode of the CH$_2$ groups, ν(CH$_2$), appears as a shoulder at 357 meV. The peak at 15 mV is due to vibrations from either Si, Au or

---

[6] The symbols δ, γ and ν denote in-plane rocking (r) and scissoring (s), out-of-plane wagging (w) and twisting (t), and stretching modes, respectively.
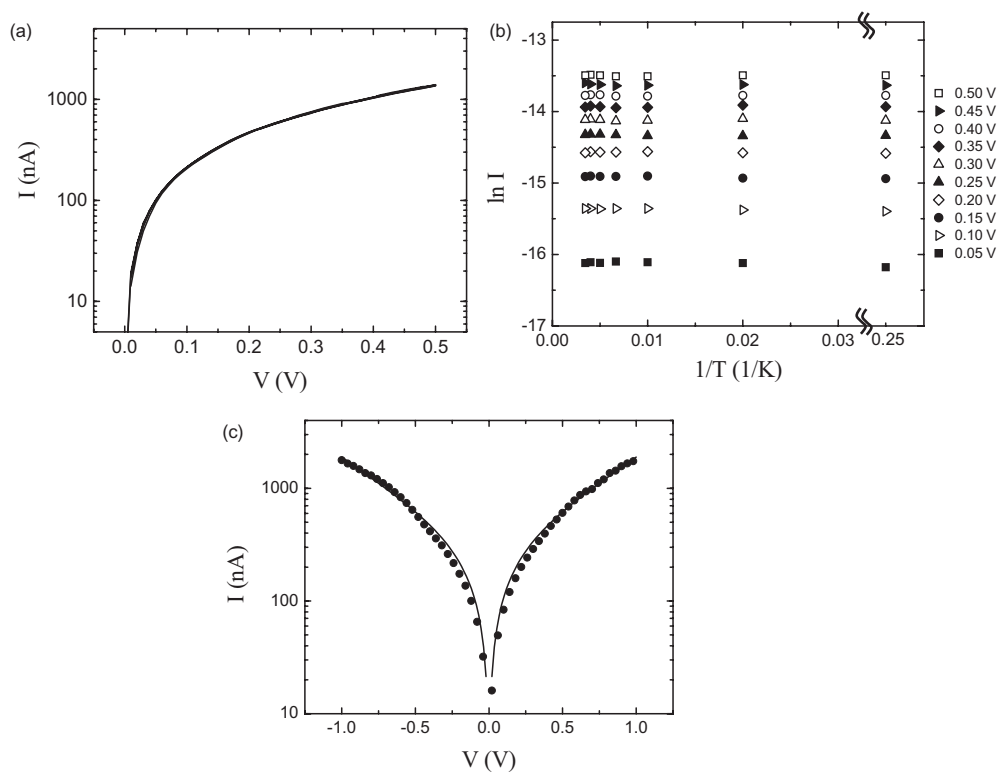
Figure 10. (*a*) $I(V, T)$ characteristics of C8-dithiol SAM at selected temperatures (4.2, 50, 100, 150, 200, 250 and 290 K). (*b*) Arrhenius plot generated from the data in (*a*), at voltages from 0.1 to 0.5 V with 0.05 V steps. (*c*) Measured C8-dithiol $I(V)$ data at room temperature (●) are compared with calculation (——) using the optimum fitting parameters of $\Phi_B = 1.20$ eV and $\alpha = 0.59$.
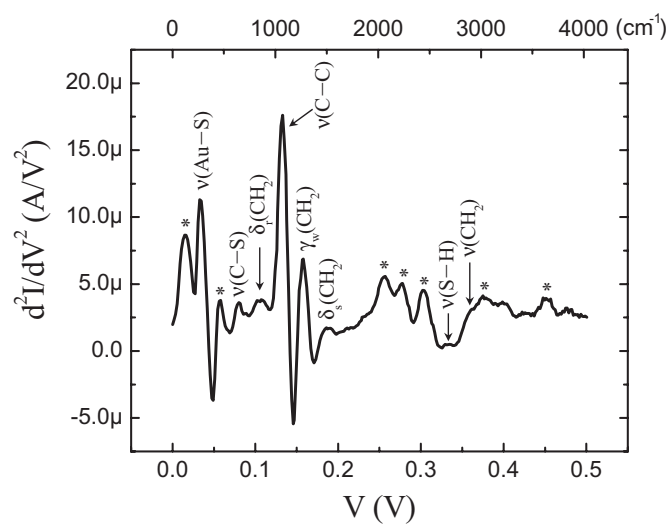

Figure 11. Inelastic electron tunnelling spectrum of C8-dithiol SAM obtained from lock-in second harmonic measurement with an ac modulation of 8.7 mV (rms value) at a frequency of 503 Hz ($T = 4.2$ K). Peaks labelled ∗ are most probably background due to the encasing Si_3N_4.

Table 4. Summary[a] of the major vibrational modes of alkanethiolates. Taken from [58–60].

Modes	Methods	Wavenumber (cm^{-1})	Bias (meV)
ν(Au–S)	HREELS[61]	225	28
ν(C–S)	Raman[60]	641	79
	Raman[60]	706	88
δ_r(CH$_2$)	HREEL[61]	715	89
	IR[62]	720	89
	IR[62]	766	95
	IR[62]	925	115
ν(C–C)	HREEL[61]	1050	130
	Raman[60]	1064	132
	Raman[60]	1120	139
$\gamma_{w,t}$(CH$_2$)	IR[62]	1230	152
	HREELS[61]	1265	157
	IR[62]	1283	159
	IR[62]	1330	165
δ_s(CH$_2$)	HREELS[61]	1455	180
ν(S–H)	Raman[60]	2575	319
ν_s(CH$_2$)	Raman[60]	2854	354
	HREELS[61]	2860	355
ν_{as}(CH$_2$)	Raman[60]	2880	357
	Raman[60]	2907	360
	HREELS[61]	2925	363

[a] There is a vast amount of literature with spectroscopic assignments for alkanethiols. The references given are representative for IR, Raman and HREELS assignments.

δ(C–C–C) [61]. We note that all alkanethiolate peaks, without exception or omission, occur in the spectra. Peaks at 58, 257, 277 and 302, as well as above 375 mV are likely to originate from Si–H and N–H vibrations related to the silicon nitride membrane [61, 62], which forms the SAM encasement. To the best of our knowledge alkanethiols have no vibrational signatures in these regions. Measurement of the background spectrum of an 'empty' nanopore device with only gold contacts to obtain background contributions from Si$_3$N$_4$ is hampered by either too low (open circuit) or too high (short circuit) currents in such a device. A similar IETS result has also been obtained, using a different test structure, recently [63].

Although there are no selection rules in IETS as there are in IR and Raman spectroscopy, certain selection preferences have been established. According to the IETS theory [64], molecular vibrations with net dipole moments perpendicular to the interface of the tunnelling junction have stronger peak intensities than vibrations with net dipole moments parallel to the interface (for dipoles close to the electrodes). Thus, vibrations perpendicular to the electrode interface, i.e. ν(Au–S), ν(C–S), ν(C–C) and γ_w(CH$_2$), dominate the IETS spectrum while modes parallel to the interface, i.e. $\delta_{r,s}$(CH$_2$) and ν(CH$_2$), are weak, as clearly shown in figure 11.

4.2.2. Linewidth study. In order to verify that the observed spectra are indeed valid IETS data, the peak width broadening was examined as a function of temperature and modulation voltage. IETS was performed with different ac modulations at a fixed temperature, and at different temperatures with a fixed ac modulation. Figure 12(*a*) shows the modulation dependence of the IETS spectra obtained at 4.2 K, and figure 12(*b*) shows the modulation
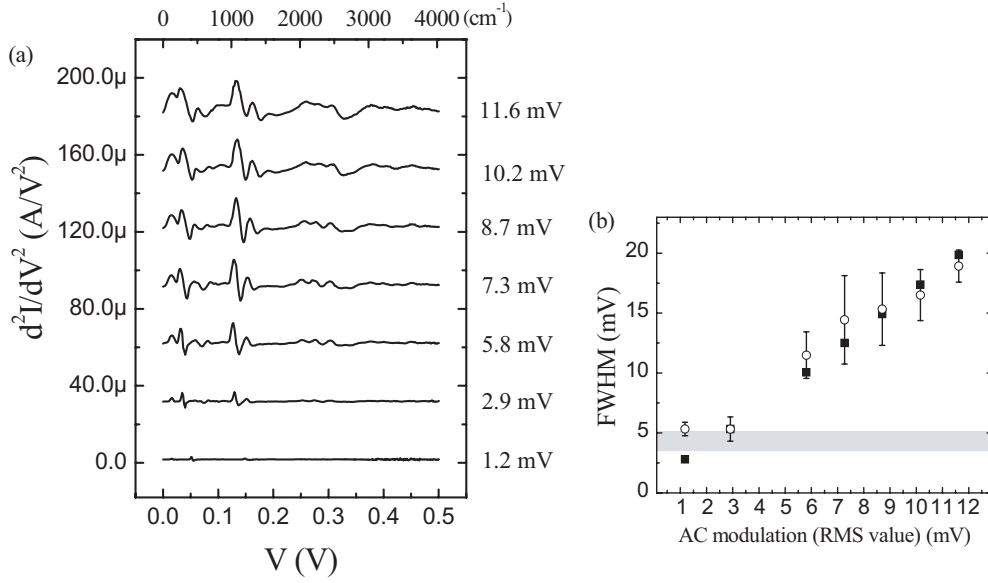
Figure 12. (*a*) Modulation dependence of IETS spectra obtained at 4.2 K. (*b*) Line (C–C stretching mode) broadening as a function of ac modulation. The circular symbols are experimental FWHMs and the square symbols are theoretical calculations considering both modulation and thermal contributions. The shaded bar denotes the expected saturation due to the derived intrinsic linewidth (including a $5.4k_BT$ thermal contribution) of 3.73 ± 0.98 meV.

broadening of the C–C stretching mode at 133 meV. The circular symbols are the full widths at half maximum (FWHMs) of the experimental peak at $T = 4.2$ K with various modulation voltages. A Gaussian distribution function was utilized to obtain a FWHM and the error range [65]. The square symbols are calculated FWHM values ($W_{\text{theoretical}}$) taking into account both a finite temperature effect ($W_{\text{thermal}} \sim 5.4k_BT$) [35] and a finite voltage modulation effect ($W_{\text{modulation}} \sim 1.7V_{\text{ac\_rms}}$) [66]. These two broadening contributions add as the squares: $W_{\text{theoretical}}^2 = W_{\text{thermal}}^2 + W_{\text{modulation}}^2$. The agreement is excellent over most of the modulation range, but we note a saturation of the linewidth at low modulation bias indicating the influence of a non-negligible intrinsic linewidth. Taking into account the known thermal and modulation broadenings, and including the intrinsic linewidth (W_I) [67] as a fitting parameter, the measured peak width (W_{exp}) is given by

$$W_{\text{exp}} = \sqrt{W_I^2 + W_{\text{thermal}}^2 + W_{\text{modulation}}^2}, \tag{6}$$

W_I can be determined by using a nonlinear least squares fit to the ac modulation data (figure 12) with equation (6), giving an intrinsic linewidth of 3.73 ± 0.98 meV for this line. This is shown (with the error range) in figure 12(*b*) as a shaded bar, including the thermal contribution.

We can independently check the thermal broadening of the line at fixed modulation. Figure 13(*a*) shows the temperature dependence of the IETS spectra obtained with an ac modulation of 8.7 mV (rms value). In figure 13(*b*) the circular symbols (and corresponding error bars) are experimental FWHM values of the C–C stretching mode from figure 13(*a*), determined by a Gaussian fit (and error of the fit) to the experimental lineshape. For simplicity we have only considered Gaussian lineshapes [65] resulting in increased error bars for the lower temperature range due to an asymmetric lineshape. The square symbols are theoretical calculations taking into account thermal broadening, modulation broadening and the intrinsic
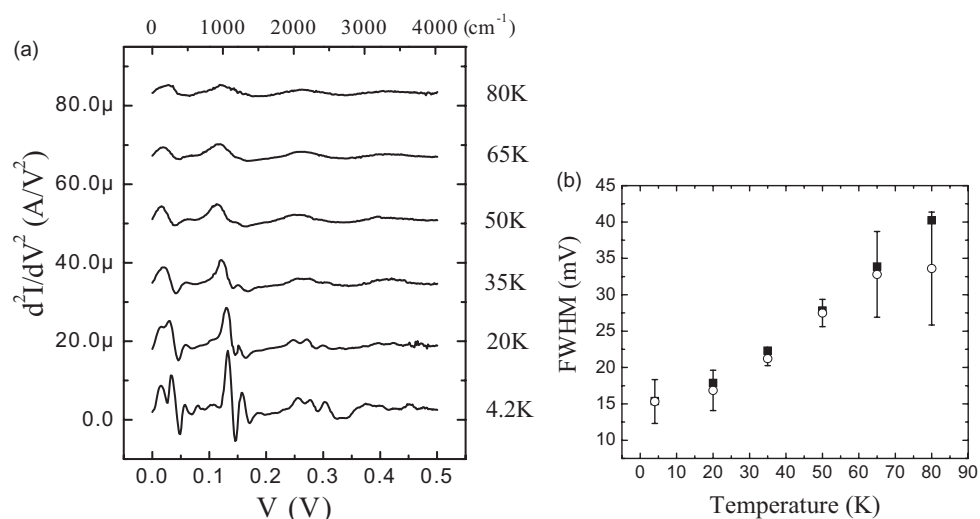
Figure 13. (*a*) Temperature dependence of IETS spectra obtained at a fixed ac modulation of 8.7 mV (rms value). (*b*) Line (C–C stretching mode) broadening as a function of temperature. The circular symbols are experimental FWHMs and the square symbols are theoretical calculations considering thermal broadening, modulation broadening and the intrinsic linewidth.

linewidth determined above. The error ranges of the calculation (due to the intrinsic linewidth error) are approximately the size of the data points. The agreement between theory and experiment is very good, spanning a temperature range from below ($\times 0.5$) to above ($\times 10$) of the thermally broadened intrinsic linewidth. This linewidth should be a sensitive test to compare with theoretical models of transmission probabilities [68].

Similar intrinsic linewidths have been determined for the Au–S stretching mode (33 meV) and the CH_2 wagging mode (158 meV), and the results are shown in figure 14. For the Au–S stretching mode, the deviation of experimental data from calculated values (thermal and modulation width only) is little (figure 14(*a*)), indicating that its intrinsic linewidth is small. A linewidth upper limit of 1.69 meV is determined for this vibrational mode. For the CH_2 wagging mode, a nonlinear least squares fit to equation (6) (solid curve in figure 14(*b*)) gave an intrinsic linewidth of 13.5 ± 2.4 meV. The linewidths and their variation throughout the molecule are potentially due to the inhomogeneous configuration of the molecular constituents, and a more detailed understanding may give detailed structural information of these device structures.

5. Conclusions

We present here a study of electron tunnelling through alkanethiol SAMs, with the intent that this system can serve as a simple standard for the development of well-characterized molecular junctions. The characteristics are consistent with accepted models of M–I–M tunnelling junctions, and thus we have a system on which tunnelling spectroscopy can be performed.

The field of 'molecular electronics' is rich in the proposal and promise of numerous device concepts [69, 70] but unfortunately there is an absence of reliable data and characterization techniques upon which to test these ideas. It is incumbent upon the experimentalist to carefully institute controls to validate claims of intrinsic molecular behaviour. Systematic controls, such
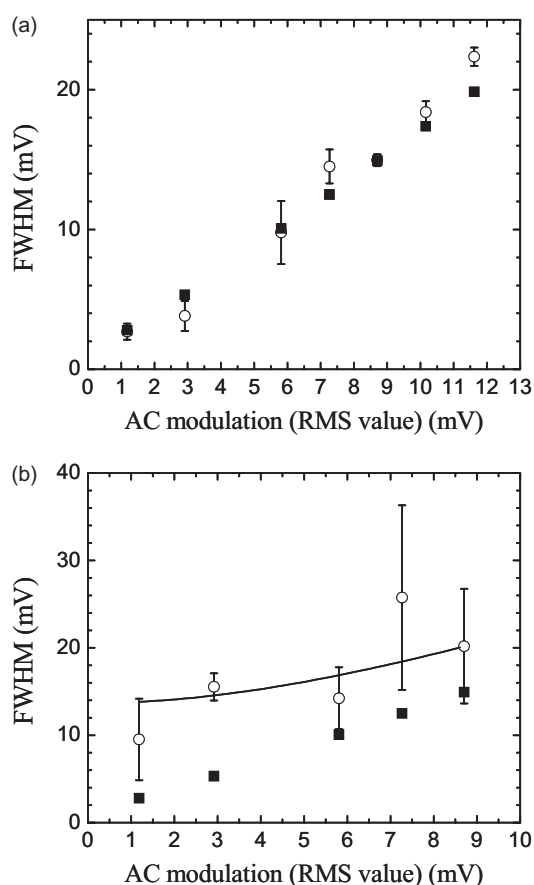
Figure 14. Line broadenings as function of ac modulation for IETS spectra obtained at 4.2 K for (*a*) the Au–S stretching mode and (*b*) the CH_2 wagging mode. The circular symbols are experimental FWHMs and the square symbols are theoretical calculations considering modulation and thermal contributions. Nonlinear least squares fitting to determine intrinsic linewidth is shown as the solid curve in (*b*). The intrinsic linewidths obtained for the Au–S stretching mode are <1.69 meV, and for the CH_2 wagging mode are 13.5 ± 2.4 meV.

as the model system presented here, should assist in guiding further work towards a rational development of fascinating device structures and systems that the field promises.

Acknowledgments

References

[1] Reed M A and Tour J M 2000 *Sci. Am.* 86–93
[2] Reed M A, Zhou C, Muller C J, Burgin T P and Tour J M 1997 *Science* **278** 252–4

[3] Reed M A and Lee T (ed) 2003 *Molecular Nanoelectronics* (Stevenson Ranch, CA: American Scientific)

[4] Heath J R and Ratner M A 2003 *Phys. Today* 43–9
Nitzan A and Ratner M A 2003 *Science* **300** 1384–9

[5] Chen Y, Jung G-Y, Ohlberg D A A, Li X, Stewart D R, Jeppesen J O, Nielsen K A, Stoddart J F and Williams R S 2003 *Nanotechnology* **14** 462–8
Beyond Silicon: Breakthroughs in Molecular Electronics, http://www.hpl.hp.com/research/qsr/ (Hewlett-Packard Quantum Science Research)

[6] Luo Y, Collier C P, Jeppesen J O, Nielsen K A, DeIonno E, Ho G, Perkins J, Tseng H-R, Yamamoto T, Stoddart J F and Heath J R 2002 *Chem. Phys. Chem.* **3** 519–25
Collier C P, Mattersteig G, Wong E W, Luo Y, Beverly K, Sampaio J, Raymo F M, Stoddart J F and Heath J R 2000 *Science* **289** 1172–5

[7] Stewart D R, Ohlberg D A A, Beck P A, Chen Y, Williams R S, Jeppesen J O, Nielsen K A and Stoddart J F 2004 *Nano Lett.* **4** 133–6
Lau C N, Stewart D R, Williams R S and Bockrath M 2004 *Nano Lett.* **4** 569–72

[8] Lee T, Wang W, Klemic J F, Zhang J J, Su J and Reed M A 2004 *J. Phys. Chem.* B **108** 8742–50

[9] Ulman A 1991 *An Introduction to Ultrathin Organic Films from Langmuir-Blodgett to Self-Assembly* (Boston, MA: Academic)

[10] Poirier G E 1997 *Chem. Rev.* **97** 1117–27

[11] Ratner M A, Davis B, Kemp M, Mujica V, Roitberg A and Yaliraki S 1998 *Molecular Electronics: Science and Technology, The Annals of the New York Academy of Sciences* vol 852, ed A Aviram and M Ratner (New York: The New York Academy of Sciences)

[12] Boulas C, Davidovits J V, Rondelez F and Vuillaume D 1996 *Phys. Rev. Lett.* **76** 4797–800
Fujihira M and Inokuchi H 1972 *Chem. Phys. Lett.* **17** 554–6
Lias S G, Bartmess J E, Liebman J F, Holmes J L, Levin R D and Mallard W G 1998 Gas-phase ion and neutral thermochemistry *J. Phys. Chem. Ref. Data* **17** 24
Yang H-H and McCreery R L 1999 *Anal. Chem.* **71** 4081

[13] Walczak M W, Chung C, Stole S M, Widrig C A and Porter M D 1991 *J. Am. Chem. Soc.* **113** 2370–8

[14] Nuzzo R G, Zegarski B R and Dubois L H 1987 *J. Am. Chem. Soc.* **109** 733–40

[15] Widrig C A, Chung C and Porter M D 1991 *J. Electroanal. Chem.* **310** 335–59

[16] Poirier G E and Tarlov M J 1994 *Langmuir* **10** 2853–6

[17] Porter M D, Bright T B, Allara D L and Chidsey C E D 1987 *J. Am. Chem. Soc.* **109** 3559–68

[18] Bumm L A, Arnold J J, Dunbar T D, Allara D L and Weiss P S 1999 *J. Phys. Chem.* B **103** 8122–7

[19] Xu B and Tao N J 2003 *Science* **301** 1221–3

[20] Wold D J and Frisbie C D 2001 *J. Am. Chem. Soc.* **123** 5549–56

[21] Wold D J, Haag R, Rampi M A and Frisbie C D 2002 *J. Phys. Chem.* B **106** 2813–6

[22] Cui X D, Zarate X, Tomfohr J, Sankey O F, Primak A, Moore A L, Moore T A, Gust D, Harris G and Lindsay S M 2002 *Nanotechnology* **13** 5–14

[23] Cui X D, Primak A, Zarate X, Tomfohr J, Sankey O F, Moore A L, Moore T A, Gust D, Nagahara L A and Lindsay S M 2002 *J. Phys. Chem.* B **106** 8609–14

[24] Holmlin R, Haag R, Chabinyc M L, Ismagilov R F, Cohen A E, Terfort A, Rampi M A and Whitesides G M 2001 *J. Am. Chem. Soc.* **123** 5075–85

[25] Rampi M A and Whitesides G M 2002 *Chem. Phys.* **281** 373–91

[26] Slowinski K, Fong H K Y and Majda M 1999 *J. Am. Chem. Soc.* **121** 7257–61

[27] York R L, Nguyen P T and Slowinski K 2003 *J. Am. Chem. Soc.* **125** 5948–53

[28] Kushmerick J G, Holt D B, Pollack S K, Ratner M A, Yang J C, Schull T L, Naciri J, Moore M H and Shashidhar R 2002 *J. Am. Chem. Soc.* **124** 10654–5

[29] Smalley J F, Feldberg S W, Chidsey C E D, Linford M R, Newton M D and Liu Y 1995 *J. Phys. Chem.* **99** 13141–9

[30] Weber K, Hockett L and Creager S 1997 *J. Phys. Chem.* B **101** 8286–91

[31] Slowinski K, Chamberlain R V, Miller C J and Majda M 1997 *J. Am. Chem. Soc.* **119** 11910–19

[32] Wang W, Lee T and Reed M A 2003 *Phys. Rev.* B **68** 035416

[33] Wang W, Lee T, Kretzschmar I and Reed M A 2004 *Nano Lett.* **4** 643–6

[34] Jaklevic R C and Lambe J 1966 *Phys. Rev. Lett.* **17** 1139–40

[35] Lambe J and Jaklevic R C 1968 *Phys. Rev.* **165** 821–32

[36] Adkins C J and Phillips W A 1985 *J. Phys. C: Solid State Phys.* **18** 1313–46

[37] Hansma P K (ed) 1982 *Tunnelling Spectroscopy: Capabilities, Applications, and New Techniques* (New York: Plenum)

[38] Stipe B C, Rezaei M A and Ho W 1998 *Science* **280** 1732–5

[39] Zhou C, Deshpande M R, Reed M A, Jones L II and Tour J M 1997 *Appl. Phys. Lett.* **71** 611–13
[40] Chen J, Reed M A, Rawlett A M and Tour J M 1999 *Science* **286** 1550–2
     Chen J, Calvet L C, Reed M A, Carr D W, Grubisha D S and Bennett D W 1999 *Chem. Phys. Lett.* **313** 741–8
[41] Ralls K S, Buhrman R A and Tiberio R C 1989 *Appl. Phys. Lett.* **55** 2459–61
[42] Metzger R M *et al* 1997 *J. Am. Chem. Soc.* **119** 10455–66
[43] Horowitz P and Hill W 1989 *The Art of Electronics* (New York: Cambridge University Press)
[44] Sze S M 1981 *Physics of Semiconductor Devices* (New York: Wiley)
[45] Thurstans R E and Oxley D P 2002 *J. Phys. D: Appl. Phys.* **35** 802–9
     Simmons J G and Verderber R R 1967 *Proc. R. Soc.* A **301** 77–102
     Dearnaley G, Stoneham A M and Morgan D V 1970 *Rep. Prog. Phys.* **33** 1129–91
[46] Mann B and Kuhn H 1971 *J. Appl. Phys.* **42** 4398–405
     Polymeropoulos E E and Sagiv J 1978 *J. Chem. Phys.* **69** 1836–47
[47] Fan F F, Yang J, Cai L, Price D W, Dirk S M, Kosynkin D V, Yao Y, Rawlett A M, Tour J M and Bard A J 2002
     J. Am. Chem. Soc. **124** 5550–60
[48] Franz W 1956 *Handbuch der Physik* vol 17 ed S Flugge (Berlin: Springer) p 155
[49] Lewicki G and Mead C A 1966 *Phys. Rev. Lett.* **16** 939–41
     Stratton R, Lewicki G and Mead C A 1966 *J. Phys. Chem. Solids* **27** 1599–604
     Parker G H and Mead C A 1968 *Phys. Rev. Lett.* **21** 605–7
[50] Brar B, Wilk G D and Seabaugh A C 1996 *Appl. Phys. Lett.* **69** 2728–30
[51] Joachim C and Magoga M 2002 *Chem. Phys.* **281** 347–52
[52] Simmons J G 1963 *J. Appl. Phys.* **34** 1793–803
[53] Simmons J G 1971 *J. Phys. D: Appl. Phys.* **4** 613–57
     Maserjian J and Petersson G P 1974 *Appl. Phys. Lett.* **25** 50–2
[54] Tomfohr J K and Sankey O F 2002 *Phys. Rev.* B **65** 245105
[55] Yamamoto H and Waldeck D H 2002 *J. Phys. Chem.* B **106** 7469–73
     Napper A M, Liu Haiying and Waldeck D H 2001 *J. Phys. Chem.* B **105** 7699–707
[56] Kaun C-C and Guo H 2003 *Nano Lett.* **3** 1521–5
[57] Piccinin S, Selloni A, Scandolo S, Car R and Scoles G 2003 *J. Chem. Phys.* **119** 6729–35
[58] Bryant M A and Pemberton J E 1991 *J. Am. Chem. Soc.* **113** 8284–93
[59] Kato H S, Noh J, Hara M and Kawai M 2002 *J. Phys. Chem.* B **106** 9655–8
[60] Castiglioni C, Gussoni M and Zerbi G J 1991 *Chem. Phys.* **95** 7144–9
[61] Molinari M, Rinnert H, Vergnat M and Weisbecker P 2003 *Mater. Sci. Eng.* B 101, 186
     Bogdanoff P D, Fultz B and Rosenkranz S 1999 *Phys. Rev.* B **60** 3976–81
     Mazur U and Hipps K W 1982 *J. Phys. Chem.* **86** 2854–60
[62] Mazur U and Hipps K W 1981 *J. Phys. Chem.* **85** 2244–9
     Kurata H, Hirose M and Osaka Y 1981 *Japan. J. Appl. Phys.* **20** L811
[63] Kushmerick J G, Lazorcik J, Patterson C H, Shashidhar R, Seferos D S and Bazan G C 2004 *Nano Lett.* **4**
     639–42
[64] Kirtley J and Hall J T 1980 *Phys. Rev.* B **22** 848–56
[65] Lauhon I J and Ho W 1999 *Phys. Rev.* B **60** R8525–8
[66] Klein J, Léger A, Belin M, Défourneau D and Sangster M J L 1973 *Phys. Rev.* B **7** 2336–48
[67] Lauhon L J and Ho W 2001 *Rev. Sci. Instrum.* **72** 216–23
[68] Kastner M A 1993 *Phys. Today* 24–31
[69] Aviram A and Ratner M (ed) 1998 *Molecular Electronics: Science and Technology, The Annals of the New York
     Academy of Sciences* vol 852 (New York: The New York Academy of Sciences)
[70] Reimers J, Picconatto C, Ellenbogen J and Shashidhar R 2003 *Molecular Electronics III, The Annals of the
     New York Academy of Sciences* vol 1006 (New York: The New York Academy of Sciences)